PAPER

Check for updates

A solid-state integrated photo-supercapacitor based on ZnO nanorod arrays decorated with Ag$_2$S quantum dots as the photoanode and a PEDOT charge storage counter-electrode†

D. Solís-Cortés, [ID] *[a] E. Navarrete-Astorga, [ID] [a] R. Schrebler,[c] J. J. Peinado-Pérez,[a] F. Martín,[a] J. R. Ramos-Barrado[a] and E. A. Dalchiele[b]

A planar solid-state photocapacitor with two electrodes has been prepared for the first time using a passivated film of ZnS with Ag$_2$S quantum dots deposited on ZnO nanorods, which were electrochemically grown on ZnO seed layers, as the photoanode. The supercapacitor part is composed of a electrodeposited poly(3,4-ethylene-dioxythiophene) PEDOT film as the counter-electrode and an ionic liquid-based electrolyte between them deposited by the dip coating method. The different nanostructures and electrodes were morphologically and structurally characterized, and the device was electrochemically characterized and could reach a potential of 0.33 V during photocharge and a storage efficiency of 6.83%.

1. Introduction

Solar photovoltaic energy conversion depends heavily on ambient factors and weather conditions (such as light intensity and day–night cycles), making the availability of solar photovoltaic power intermittent and many times unreliable.[1–3] These problems impel the use of energy storage devices, which help mitigate the power output swing during generation.[2–5] As solar cells of all types are unable to store the converted energy for further use, usually external energy storage devices, such as batteries and electrochemical capacitors (supercapacitors), are used in combination with solar cells.[2,5–7] In recent years, due to their elevated energy efficiency, quick rechargeable capacity, long cycle life and low maintenance costs, supercapacitors have drawn growing attention among the different energy storage systems.[3,5,8–12] In fact, electrochemical supercapacitors with high power density, fast charge/discharge rate (in seconds) and stable cycling performance have attained great research interest for applications in hybrid electric vehicles, portable consumer electronics and solar power plants.[2,5] Moreover, the electrode materials used in supercapacitors are often cost-effective and

non-toxic, making them convenient for users and environmentally friendly.[2,5,6,11–13] Usually, the photoenergy converter and energy storage devices are separately operated, resulting in some space and energy consumption by the external connection system, thereby reducing the storage efficiency of the supercapacitor part.[2,6,9,14,15] In order to alleviate this problem, significant efforts have been made to develop new integrated energy systems that combine the functions of both photovoltaic cells and energy storage units into a single device for high efficiency, lightweight, flexibility and portability.[2,4,9,14] In this sense, devices that combine solar cells and supercapacitors for both solar energy capture and electrochemical energy storage in the same device are referred to as photo-supercapacitors or solar capacitors.[3,5,15–20] For manufacturing these integrated "photo-charging" energy systems, multiple solar cells technologies (*e.g.*, dye-sensitized, organic, perovskite, and silicon) for the solar cell part and super-capacitors types (double layer, pseudo-capacitors, and hybrid) for the storage part have been combined following different approaches.[3,5,7,14,16–19,21,22] At present, most of the integrated photo-supercapacitors are based on dye-sensitized solar cells and capacitors.[7,15,17,18,21–23] However, to date, the integration of a quantum dot solar cell (QDSC) and a supercapacitor has hardly been reported, and the literature on this topic is scarce.[3,7,15,17,18,21–23] In fact, only a couple of works dealing with photo-supercapacitors based on photoanodes made of TiO$_2$ mesoporous layers sensitized by CdS and CdS/CdS quantum dots (QDs) are found in the literature.[24,25] In this configuration, the QD-based photoanode converts solar energy into electric current, and this current is utilized to charge the supercapacitor.[24,25] In this paper, a ZnO nanorod (NRs) array

[a]Universidad de Málaga, Andalucía Tech, Departamentos de Física Aplicada & Ingeniería Química, Laboratorio de Materiales y Superficies (Unidad Asociada al CSIC), E29071 Málaga, Spain. E-mail: dsolis@uma.es; Tel: +34 952131920

[b]Instituto de Física, Facultad de Ingeniería, Herrera y Reissig 565, C.C. 30, 11000 Montevideo, Uruguay

[c]Instituto de Química, Facultad de Ciencias, Pontificia Universidad Católica de Valparaíso, Casilla 4059, Valparaíso, Chile

† Electronic supplementary information (ESI) available. See DOI: 10.1039/c9ra10635a

decorated with Ag_2S QDs and one-dimensional architecture was employed as the exciton generator (the solar cell part of the photo-supercapacitor). Zinc sulphide (ZnS) was deposited over Ag_2S in order to passivate the surface and avoid recombination.[26] The energy band structure and physical properties of ZnO are similar to those of TiO_2,[27,28] whereas its electron mobility is higher (ZnO, 115–155 cm^2 V^{-1} s^{-1}; TiO_2 10^{-5} cm^2 V^{-1} s^{-1}).[27,28] Consequently, ZnO is expected to exhibit faster electron transport with less recombination loss.[27,28] Furthermore, ZnO is considered as the most promising alternative to TiO_2 due to its ease of crystallization and anisotropic growth.[27,28] Recently, narrow bandgap semiconductor QDs, such as Ag_2S, CdS, CdSe, CdTe, PbS, PbSe, InP, In_2S_3 and InAs, have been intensively used as sensitizers of widegap photoanodes (ZnO and TiO_2 materials) in QDSCs.[29–35] Among these, Ag_2S is an excellent choice, particularly due to its narrow band gap (1.1 eV), which is very close to the optimal band gap value of a single junction photovoltaic device (1.13 eV), and negligible toxicity.[36] On the other hand, poly(3,4-ethylene-dioxythiophene) (PEDOT), an air- and thermal-stable, environmentally benign, highly transparent and highly conductive hole conducting polymer, has been widely used as the conductive electrode in flexible electronic and optoelectronic devices.[13,14,37,38] Furthermore, PEDOT exhibits a strong ability for hole transport and charge storage.[13,14,39–41] Therefore, PEDOT has been used here both as a hole transport material and as a polymeric charge storage counter-electrode. Moreover, the electrolyte is another component of the photocapacitor, which plays an important role, and should have a high ionic conductivity.

Recently, an interesting $PVP/[HEMIm][BF_4]$ solid-state and self-standing ion gel electrolyte was developed by our group and successfully tested on supercapacitors, (see more details in ESI†).[11,16] Herein, we report for the first time, a planar photo-supercapacitor with nano-architecture composed of ZnO NR arrays decorated with Ag_2S QDs as the photoelectrode (photoanode), $PVP/[HEMIm][BF_4]$ solid-state ion-gel as the electrolyte and polymeric PEDOT as the capacitor-type counter-electrode.

2. Experimental methods

2.1 Preparation of the photoelectrode

To prepare the photoelectrode part of the photocapacitor, first, ZnO nanorod arrays (NRs) (the main nanoarchitecture of the photo-storage device) were electrochemically grown onto zinc oxide thin film seed layers (SLs) deposited onto transparent substrates, which consisted of glass plates with a conductive thin film of fluorine-doped tin oxide (SnO_2:F, FTO) on one side (Pilkington TEC Glass, sheet resistance of about 8 Ω $\square^{-1}$). The FTO/glass substrates were first cleaned by ultrasonication for 15 minutes each in acetone, 2-propanol and de-ionized water. To form the zinc oxide seed layer on each electrode, 1 mL of a $Zn(CH_3COO)_2$ (10 mM) methanolic solution was added dropwise via spin-coating (2000 rpm) for 40 seconds, and then, the sample was dried at 105 °C for 10 min. This process was repeated four times. Finally, an annealing treatment was performed under air at 350 °C for

20 min with a temperature/time ramp of 10 °C min^{-1}. Substrates obtained following the above-described procedure were known as the one zinc oxide seed layers (1SL). Subsequently, on repeating this procedure on the prepared zinc oxide 1SL modified-FTO/glass substrate, in the second cycle, the corresponding zinc oxide 2SL FTO/glass substrates were obtained. ZnO nanorod arrays were grown from a 1 mM zinc acetate aqueous solution maintained at 70 °C by the electrochemical deposition method. As the supporting electrolyte, 0.1 M sodium acetate was employed to ensure good electrical conductivity in the aqueous solution (Milli-Q quality water, 18 $M\Omega$ cm^{-1}). The pH of the solution was initially adjusted to 6.76. Electrodeposition was performed in a conventional three-electrode electrochemical cell with the substrate as the working electrode, a platinum sheet as the counter electrode and a saturated calomel electrode (SCE) as the reference. Electrodeposition was carried out potentiostatically at −1.0 V vs. SCE. The electrolyte was saturated with pure molecular oxygen by continuous bubbling starting 45 min prior to electrodeposition and during the growth process. The electrochemical deposition time was 3600 s. After electrodeposition, the ZnO NRs/ZnO SL/FTO/glass substrate samples were thoroughly and carefully rinsed with DI water to remove unreacted products from the surface and dried under a moderate air flux. The ZnO NRs were selected based on the best condition determined from the experimental optimization performed previously: $[ZnAc_2]$ = 1 mM, T = 70 °C, t = 60 min.

Then, the ZnO nanowire arrays were decorated with Ag_2S QDs through the facile successive ionic layer adsorption and reaction (SILAR) method. The ZnO nanorod array samples were successively immersed for 1 min each in two different non-aqueous solutions, one containing Ag^+ cations (50 mM $AgNO_3$ in ethanol) and the other one containing S^{2-} anions (50 mM Na_2S in methanol). After the Ag^+ and S^{2-} dipping periods, the sample was rinsed for 40 s with ethanol (after cationic dipping) and methanol (after anionic dipping), respectively, to remove the excess ions weakly bound to the nanorod surface. This procedure completed one SILAR cycle. This Ag_2S QD decoration process was repeated for 9 SILAR cycles. Then, thermal annealing was carried out at 400 °C for 1 hour in an N_2 atmosphere. Finally, the ZnO NRs decorated with Ag_2S QDs were passivated by the deposition of a thin ZnS layer. The passivating ZnS layer was coated onto the ZnO/Ag_2S QD nanostructures using the SILAR method as well. To this end, the ZnO/Ag_2S nanostructured samples were successively immersed in two different aqueous solutions for 1 min each, one containing Zn^{2+} cations (0.5 M of $Zn(CH_3COO)_2$) and the other containing S^{2-} anions (0.5 M Na_2S). Between each Zn^{2+} and S^{2-} dipping period, the sample was rinsed with water for 40 s to remove the non-adsorbed/unreacted ions. This SILAR coating cycle was repeated 4 times. PEDOT was electrodeposited on this structure to act as the hole transporting material and as a shared electrode between the photoelectrode and the counter-electrode. Fig. 1 shows the different steps in the fabrication of the photoelectrode part of the photocapacitor.
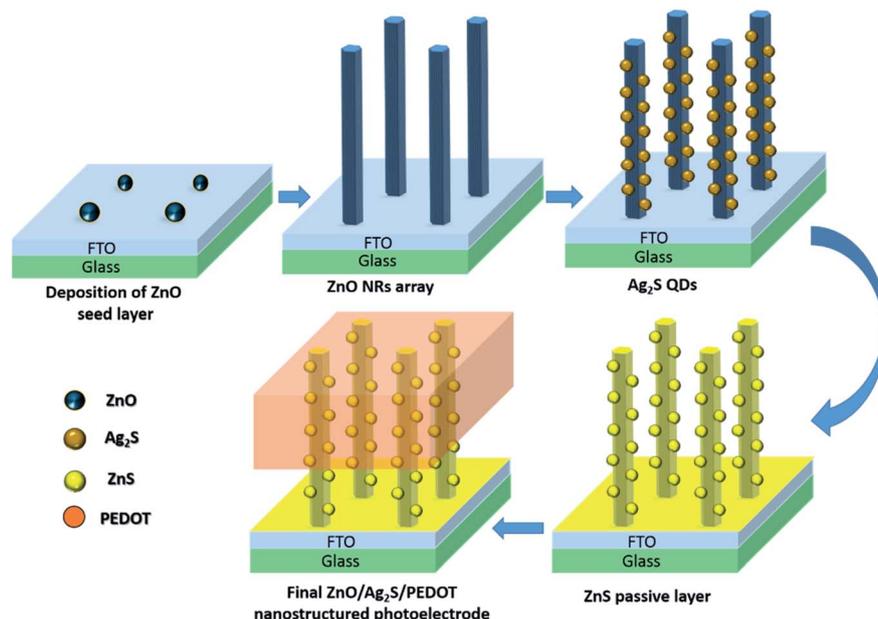
Fig. 1 Schematic of the fabrication process of the designed nanostructured photoelectrode for the integrated photo-supercapacitor device.

2.2 Supercapacitor part preparation

PEDOT was synthesized by the electropolymerization of EDOT over commercial FTO/glass substrates by employing 5 cycles of cyclic voltammetry. Once PEDOT was electrodeposited on one side of the FTO glass substrate, it was dipped in an ionic liquid solution composed of methanol, PVP and [HEMIm][BF$_4$].

2.3 Assembly of QDSSC with supercapacitor to form the integrated two-electrode photo-supercapacitor

Once the photoanode and the supercapacitor were constructed, they were assembled with a polymer separator (Solaronyx, 25 μm thickness) (size: 0.5 cm × 0.5 cm) sandwiched between the QDSSC and the counter-electrode. Both parts were connected due to the high viscosity of the electrolyte. After a while, the parts remained totally bounded, thus completing the device.

2.4 Material characterization

The structural characterization of the photoelectrode was carried out by X-ray diffraction (XRD) on a PANanalytical X'Pert Pro automated diffractometer. Patterns were recorded in the Bragg–Brentano configuration using a monochromatic high intensity (Cu Kα1) radiation. An X'Celerator detector with a step size of 0.017° (2θ) was used, and the working power was 45 kV × 40 mA. The oxidation state of the chemical elements was studied *via* X-ray photoelectron spectroscopy (XPS) using an ESCA 5701 from Physical Electronics (PHI). An Mg Kα radiation source (15 eV) with an operating power of 400 W in an ultra-high vacuum system at a base pressure of ~1.3 × 10^{-8} Pa was employed. Topographic AFM examinations were performed by using a Nanoscope V tapping-mode AFM (Veeco Instruments) employing sharp silicon tips.

Field emission scanning electron microscopy (FE-SEM) images of the electrodes were obtained on a Helios Nanolab 650 Dual Beam equipment from FEI Company. High-resolution transmission electron microscopy (HRTEM) images were obtained on a Talos F200X instrument.

The electrochemical behavior of the resulting photo-supercapacitor was evaluated by cyclic voltammetry (CV), galvanostatic charge–discharge (GCD) measurements and electrochemical impedance spectroscopy (EIS) carried out at room temperature with a Biologic VSP potentiostat.

For the investigation of the photovoltaic supercapacitor performance of the photo-supercapacitor, illumination was provided by a 500 W Oriel xenon lamp with a solar filter AM1.5G, and the incident illumination power at the electrode surface was about 100 mW cm^{-2}.

3. Results and discussion

3.1 Structural and morphological properties of the ZnS/Ag$_2$S/ZnO photoanode

The working principle of this photocapacitor is shown in Fig. 2; the red and green arrows indicate the photo-charge and discharge processes of the supercapacitor, respectively. The mechanism was interpreted as follows: under light illumination, the Ag$_2$S QDs are photo-excited, and the electrons from QDs are injected into the ZnO nanorods and flow through the external circuit to the counter-electrode (PEDOT), where negative charge accumulates. At the same time, the PEDOT layer electrodeposited over the ZnO nanorods of the photoanode results in a partial positive charge. The BF^{4-} ions are attracted toward this positive charge, and the ion gel cations [HemIm]$^+$ go to the PEDOT/FTO layer, which is the negatively charged cathode, producing the
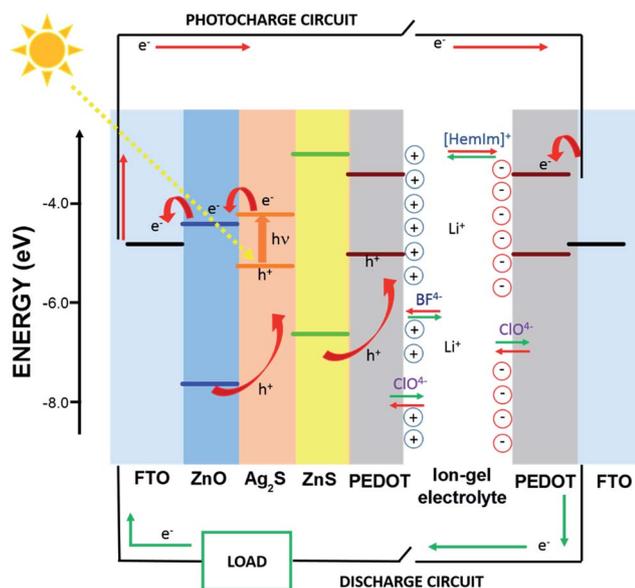
Fig. 2 Schematic of the configuration and working mechanism of the photo-supercapacitor device.

separation of the ionic liquid electrolyte and forming a double layer. The perchlorate anion (ClO^{4-}) corresponding to the PEDOT layer suffers oxidation and reduction reactions (Fig. 5). Then, a double layer supercapacitor base is obtained. Finally, during the discharging process in darkness, the double layer reorganizes itself again. The structural and morphological characteristics of the photoanode are shown in Fig. 3. The FESEM micrograph of ZnO nanorods grown on the FTO/ZnO seed layer is shown in Fig. 3a, demonstrating a high degree of orientation along the z-axis. The top-view of the nanorods (inset) shows the characteristic hexagonal shape of the wurtzite structure. Fig. 3b shows the images of the ZnO@Ag$_2$S core–shell NRAs. After sensitization, the NR surface became rough and grainy, which was clearly visible with spherical nanoparticles surrounding them. The morphology of the ZnO nanorods before and after QD deposition was similar, which indicated that the NR structure did not change during Ag$_2$S QD growth. These results suggested that the Ag$_2$S QDs were successfully deposited onto the surface of the ZnO nanorods along their entire length, forming a ZnO/Ag$_2$S core–shell structure. Fig. 3c shows the same Ag$_2$S@ZnO NRAs covered with ZnS, demonstrating that the film covered the entire surface of the quantum dots. It has been confirmed that this ZnS film contributes to the improvement of the photoresponse.[42,43] Fig. 3d shows the tilted view of the nanostructures covered with electrodeposited PEDOT. It could be seen that PEDOT covered the surface of the nanorods, forming a uniform film.

The finer details of the Ag$_2$S@ZnO NRAs core–shell microstructure were further investigated by high-resolution transmission electron microscopy (HRTEM), as illustrated in Fig. 4a and b. A single Ag$_2$S QD/ZnO NR detached from the ZnO seed layer substrate and the large number of QDs deposited onto the
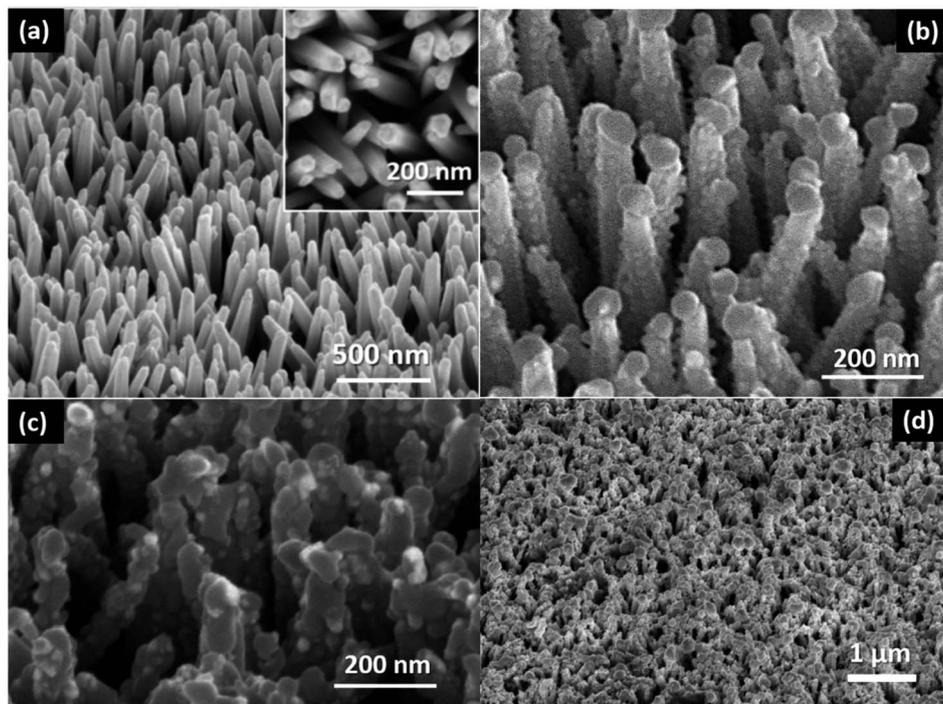

Fig. 3 (a) Tilted FESEM micrograph of bare ZnO nanorod arrays electrochemically grown on a FTO/glass substrate. The inset of (a) shows the high magnification top view image of the ZnO nanorod arrays. (b) Tilted FESEM micrograph of the ZnO nanorod arrays after decoration with Ag$_2$S QDs. (c) Tilted FESEM image of ZnS covering the Ag$_2$S QDs@/ZnO NR nanostructure. (d) Tilted FESEM micrograph showing the PEDOT layer grown on the ZnS@Ag$_2$S QDs@ZnO NR nanostructure.
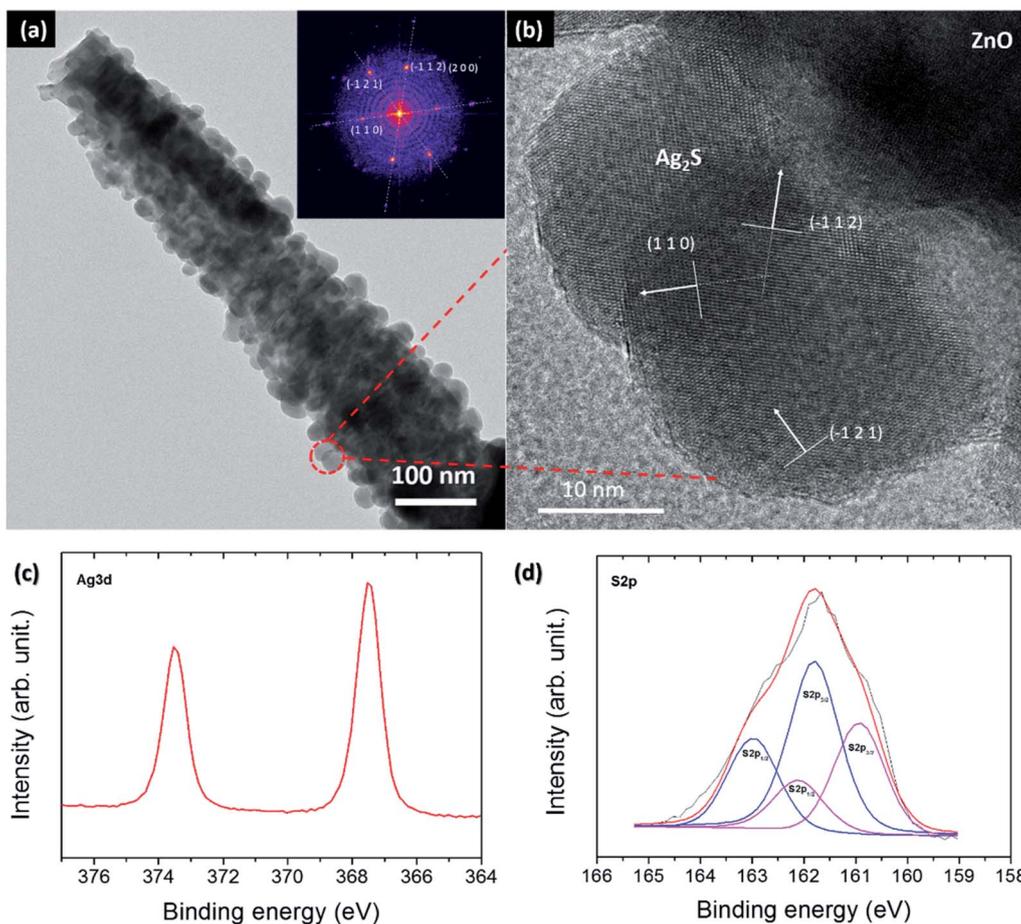
Fig. 4 (a) HRTEM image of a single ZnO nanorod decorated with Ag$_2$S QDs. The inset shows the FFT pattern. (b) High-magnification HRTEM image of (a) depicting individual Ag$_2$S QDs. (c) The Ag 3d region and (d) the S 2p deconvoluted curve from XPS analysis.

entire NR surface are shown (the inset displays the fast Fourier transform (FFT) image). Fig. 4b shows the magnified image of the QDs deposited on the ZnO nanorod surface. It could be observed that the Ag$_2$S QDs had a spherical shape with a mean diameter in the range of 10–20 nm. Three lattice fringes corresponding to the monoclinic (1 1 0), (−1 1 2) and (−1 2 1) planes were marked for the nanoparticles of Ag$_2$S, which were in accordance with the peaks in the XRD pattern (Fig. S1a, ESI†). Furthermore, the (1 1 0) and (−1 2 1) planes, which were not identified by routine XRD analysis, could be detected in this high-magnification HRTEM image.

The C 1s, O 1s, Zn 2p, Ag 3d and S 2p core levels were measured. Fig. 4d shows the S 2p region of the XPS spectrum. The black line represents the experimental data, and the red line corresponds to the fitted curve. This peak could be deconvoluted into four peaks corresponding to S 2p$_{3/2}$, S 2p$_{1/2}$ in ZnS and Ag$_2$S. The binding energy of the S 2p$_{3/2}$ peak located at 161.80 eV is in accordance with the binding energy of ZnS.[44–46] The lowest energy peak of S 2p$_{3/2}$ was located at 160.93 eV, corresponding to Ag$_2$S. Furthermore, the peak position of Ag 3d$_{5/2}$ was located at 367.55 eV, as seen in Fig. 4c. These values are in good agreement with the reported values for Ag$_2$S nanoparticles.[46,47]

3.2 Morphological characterization of the PEDOT electrodes

Poly(3,4-ethylenedioxythiophene) (PEDOT) was electrodeposited onto FTO and exhibited a dark blue color. It was uniform with no visible defects and had good adhesion to the FTO surface. The FE-SEM micrographs of PEDOT films deposited onto FTO substrates by the potentiostatic polymerization method are presented in Fig. 5a. The low-magnification image shows a uniform and continuous film without cracks or pinholes. The inset image depicts a high-magnification image of the film, showing a dense and rough granular layer made of round-shaped particles about 200 nm in diameter. The thickness of the PEDOT film was measured from the cross-section images from field emission-scanning electron microscopy (Fig. 5b). After 5 cycles, the average thickness of the PEDOT film was 59.6 nm. Fig. 5c shows the AFM images of PEDOT over an area of 1 μm^2. The roughness of the PEDOT electrodes grown for 5 cycles was 40.4 nm. In order to confirm the successful electrodeposition of the PEDOT thin film on the FTO/glass substrate, Raman spectroscopy was carried out. Fig. 5d shows the typical Raman spectrum of the PEDOT thin film in the wavenumber region 1800–400 cm^{-1}. In Table 1, the wavenumbers of the eleven Raman peaks and comparison with studies on undoped PEDOT based on the research of Chiu
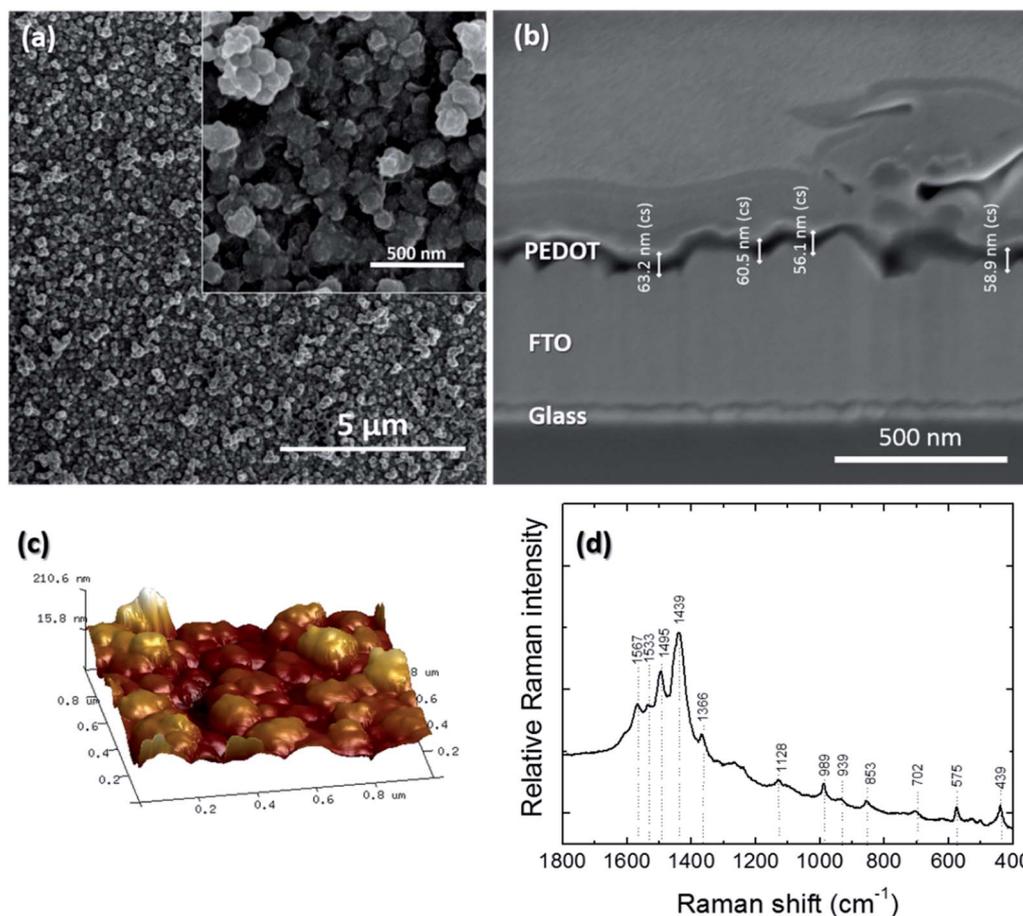
Fig. 5 (a) FE-SEM top-view image of PEDOT. Inset shows the high-magnification image of the film. (b) Cross-section image of electrodeposited PEDOT on the FTO substrate. (c) AFM image and (d) Raman spectrum (532 nm excitation) of electrochemically prepared PEDOT.

et al.,[63] Snyder et al.[48] and Louarn et al.[49] are presented. Our Raman spectrum showed a consistent match for all peaks with the corresponding Raman peaks of chemically synthesized PEDOT.[50] The shift in the position of some doped PEDOT peaks relative to those of undoped PEDOT was related to the level of doping in the conducting polymer. The most intense peak was observed at 1439 cm^{-1}, which was attributed to the $C_\alpha{=}C_\beta$ (–O) symmetric stretching vibrational modes. The asymmetric $C_\alpha{=}$

C_β stretching modes were identified by the peaks at 1495 and 1533 cm^{-1}. This indicated that in the electropolymerization process, PEDOT film formation involved long-chain linkage through α–β couplings. Therefore, the linkages at the β-position were formed *via* progressive delocalization of the unpaired electrons.[51] The position of the Raman peaks corresponding to the C_β–C_β stretching and the C_α–$C_{\alpha'}$ inter-ring stretching modes at 1366 and 1266 cm^{-1}, respectively, suggested that the cation

Table 1 Summary of PEDOT Raman vibrations at three different excitation wavelengths (532 nm, 785 nm and 1064 nm)

Excitation wavelength			
532 nm (cm^{-1}) doped PEDOT (this work)	785 nm (cm^{-1})[63] undoped PEDOT	1064 nm (cm^{-1})[48,49] undoped PEDOT	Approximate description of vibrational modes
1533	1516	1520	Asymmetric $C_\alpha{=}C_\beta$ stretching
1439	1414	1431	Symmetric $C_\alpha{=}C_\beta$ (–O) stretching
1366	1370	1369	C_β–C_β stretching
1266	1252	1226/1270	C_α–$C_{\alpha'}$ (inter-ring) stretching
1128	1097	1111	C–O–C deformation
989	990	991	Oxyethylene ring deformation
702	699	692	Symmetric C–S–C deformation
575	578	571	Oxyethylene ring deformation

radical association also occurred by the linkage at the α–α' (5,5') position, which indicated short-chain PEDOT oligomers and that the molecular structure was dominantly in the *trans* configuration with a high regiochemical order.[52] ClO_4^- ion conjugation during PEDOT growth was revealed by a broad peak at 939 cm^{-1} based on the Raman peak of free ClO_4^- at 934 cm^{-1} and that of the $[Li^+ClO_4^-]$ ion pairs at 948 cm^{-1}.[53] The anion (ClO_4^-) association in the growing chain network was caused by the positive charge in the molecular subunits of the chain, thus creating the doped state of PEDOT. Finally, from the Raman spectrum, it was concluded that conducting polymer-doped PEDOT was successfully electrodeposited onto the FTO substrates.

3.3 Electrochemical performance

Fig. 6a shows the cyclic voltammograms obtained at different scan rates (50, 100, 150 and 200 mV s^{-1}) with higher areas under the curves at higher scan rates, as expected. The shape of the curves was almost rectangular at all scan rates, indicating low resistance and good reversibility. As shown in Fig. 6b, the near-triangular shape of the galvanostatic charge–discharge curves at different current densities indicated the quasi-reversible process characteristic of the pseudocapacitor. To analyze the cyclic stability of the photocapacitor, the specific capacitance and specific energy were calculated from the CV curves obtained from 1200 cycles (Fig. 6c), and the resulting values are plotted in Fig. 6d. Specific capacitances from 0.334 mF cm^{-2} to 0.339 mF cm^{-2} were achieved under dark conditions depending on the

voltammetry cycle number. Furthermore, specific energies from 7.44 μJ cm^{-2} to 7.53 μJ cm^{-2} were obtained. Though both values decreased with the cycle number, this decrease was not very relevant considering the number of cycles (1200).

3.4 Impedance analysis

In order to study the photocapacitor device characteristics, electrochemical impedance spectroscopy (EIS) measurements were recorded at four different applied bias potentials E = 0.0 V, 0.1 V, 0.2 V and 0.3 V under dark conditions. The obtained values are depicted in Table 2. Fig. 7a and b show the typical Nyquist and Bode plots of the photocapacitor device under study at the applied bias potential E = 0.0 V. The fits indicated by solid lines in the plots showed good agreement with the data. This confirmed the suitability of the equivalent circuit model used. The Nyquist plot consisted of an incomplete small semi-circle at the higher frequency region with a non-zero intercept and a linear tail at lower frequencies. The impedance at high frequencies showed low resistive behaviour with the series resistance of 136.2 Ω at 0.0 V, which remained constant at higher applied voltages. Series resistance (R_s) represents the sheet resistance of FTO and the contact resistance of the FTO/ZnO nanorods. The semicircle with a linear tail in the Nyquist plot suggested that the polarization was due to a combination of diffusion and kinetic processes. Parallel resistance (R_p) represents the resistance to leakage currents in the photocapacitor, and their values were very high and increased with applied voltage. These results meant a low leakage current and therefore
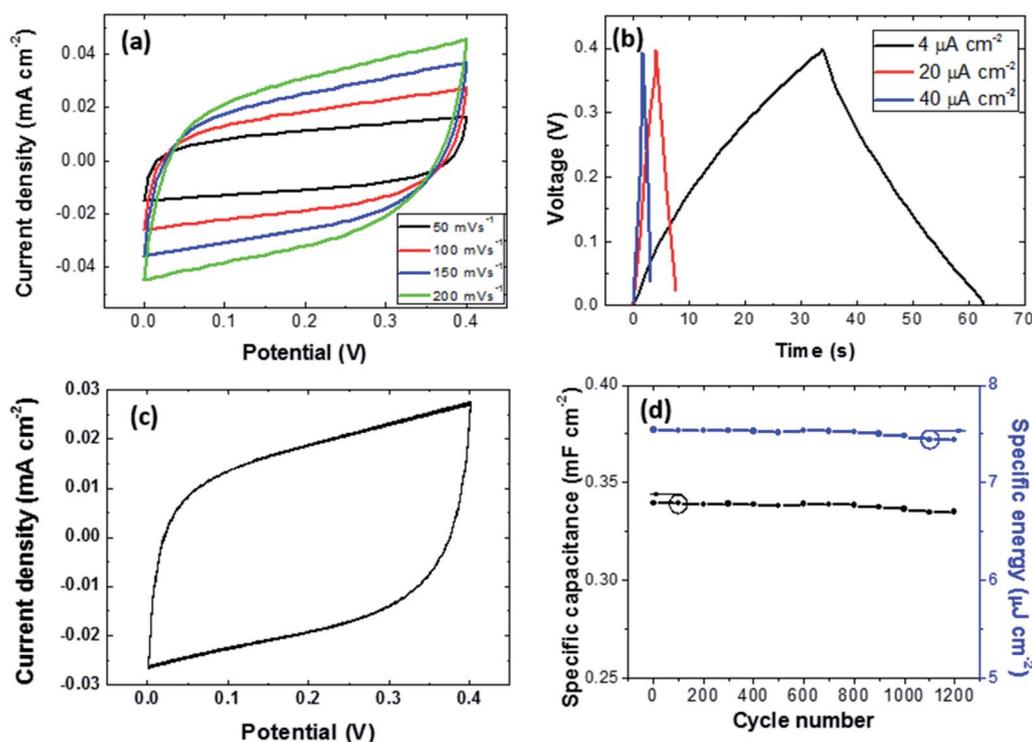

Fig. 6 (a) Cyclic voltammetry curves at different scan rates in darkness. (b) Galvanostatic charge–discharge curves at different current densities. (c) Cyclic voltammograms measured at 100 mV s^{-1} from 1200 cycles. (d) Specific capacitance (black circles) and specific energy (blue circles) values obtained from the CV curves of the photocapacitor.

Table 2 Equivalent circuit element values of the EIS spectra obtained through a complex non-linear least-squares fitting program

	Applied bias potential (V)			
	0	0.1	0.2	0.3
R_s (Ω)	136.2	157.1	155.7	154.2
CPE (S s$^\alpha$)	6.06×10^{-6}	7.5×10^{-6}	9.5×10^{-6}	1.24×10^{-5}
α	0.682	0.669	0.649	0.628
R_p (MΩ)	0.979	1.67	2.33	7.70
R_{ct} (Ω)	1063	1582	1856	2072
Q (S s^n)	8.74×10^{-6}	6.52×10^{-6}	6.70×10^{-6}	7.46×10^{-6}
n	0.835	0.826	0.832	0.844

very low electronic conductivity in the PVP/[HEMIm][BF$_4$] electrolyte. The capacitor could be equivalent to a constant phase element (CPE and Q, in this case) because both electrodes do not have a double-layer behaviour, this indicates that the supercapacitor do not correspond to an ideal capacitor.

The "n" values were nearly 1, which indicated that this QPE approached the capacitance of a rough surface of 40.4 nm, which was confirmed by the AFM characterization of the PEDOT

electrodes (Fig. 4c). The values obtained for R_{ct} were not very high and indicated an electron transfer reaction in the photoanode.

3.5 Photovoltaic supercapacitor performance

Fig. 8a shows the photocharge and galvanostatic discharge process (in dark) of the photosupercapacitor at different discharge current densities from 4 to 400 μA cm^{-2}. The device was totally photocharged to a final work potential of 0.33 V in 40 s and the process was maintained for 600 s consistently. The voltage achieved is higher than those of other photocapacitors composed of two electrodes[54,55] and even with three electrodes reported in the literature.[56] The photocharge time was lower than that reported in another study,[57] which was higher than 2000 s. After photocharge, the device was discharged at 4 μA cm^{-2} in a discharge time of 55 s, at 40 μA cm^{-2} in 2 s and at 400 μA cm^{-2} in 1 s. As expected, the discharge time decreased with the applied current density, achieving 100 s for the lowest value of current density. This discharge time was comparable to those of other photocapacitors with higher applied discharge current density.[4,58] Some cycles of photocharge and galvanostatic discharge (in dark) carried out at 4 μA cm^{-2} are presented in Fig. 8b, showing the stability of the photocapacitor through the cycling process (50 cycles). The performance of the integrated
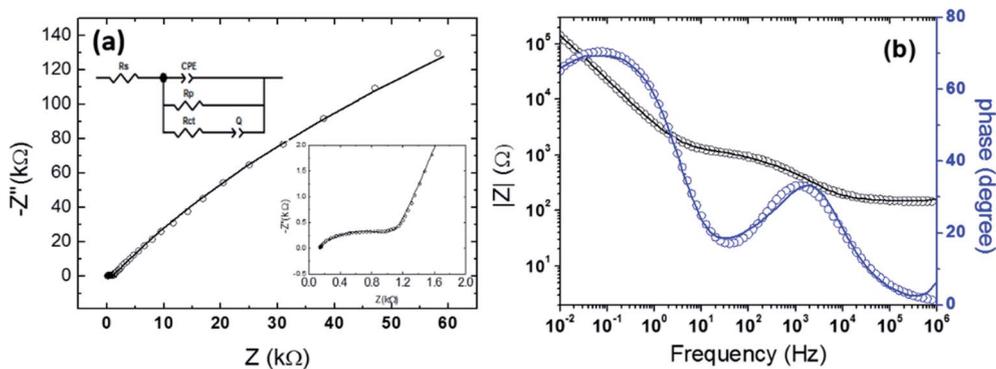

Fig. 7 (a) Nyquist and (b) Bode plots recorded for the photocapacitor device at an applied bias potential of 0.0 V under dark conditions. The symbols (open circle shapes) stand for experimental data; the solid lines are the curves fitted to the electrical circuit model depicted in the inset of (a). The inset shows the high frequency region.
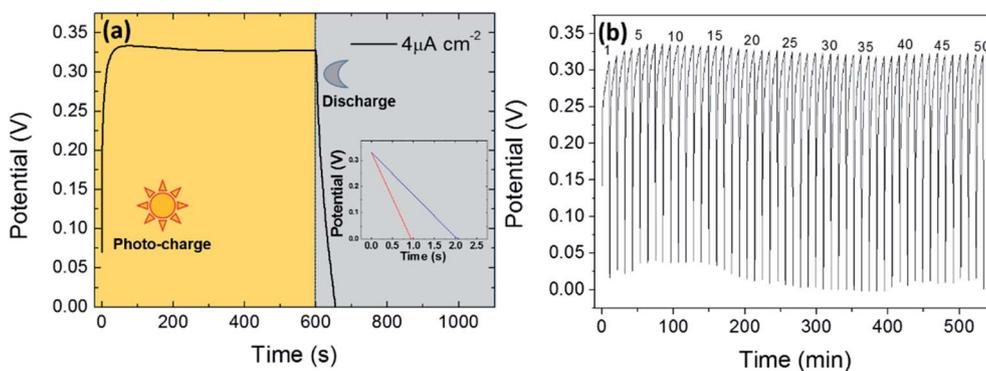

Fig. 8 (a) Photocharge under AM1.5G simulated sunlight (100 mW cm^{-2}) illumination and galvanostatic discharge at 4 μA cm^{-2} in dark conditions (inset shows the galvanostatic discharge at 40 μA cm^{-2} (blue line) and 400 μA cm^{-2} (red line) current densities). (b) Some cycles of photocharge/galvanostatic discharge at 4 μA cm^{-2}. Cycle numbers are indicated.

photocapacitor was evaluated by calculating the η_{overall} and η_{storage} values from the photocharge–discharge curves. The capacitance of the device was 0.667 mF cm^{-2}, which is higher than that reported in another work that employed ZnO as the photoelectrode and graphene as the counter-electrode[59] and in the range of another photosupercapacitor based on Bi-polar TiO$_2$ nanotubes.[60] The calculated stored energy was reached the value of 3.63×10^{-5} W h cm^{-2}. Furthermore, the integrated photocapacitor reached the maximum overall photoelectric efficiency of $\eta_{\text{overall}} = 8.25 \times 10^{-4}\%$ and maximum storage efficiency of $\eta_{\text{storage}} = 6.83\%$. Although other photocapacitors with higher efficiencies exist in the literature,[61,62] the concept of photocapacitor is promising and the device exhibits good capacitance, less photo-charge time and stability in repeated photocharge–discharge cycles. Furthermore, this two-electrode device is low in cost, environmentally friendly and easy to fabricate.

4. Conclusions

In conclusion, a two-electrode solid-state integrated photo-supercapacitor containing ZnO nanorod arrays decorated with Ag$_2$S quantum dots as the photoanode, a PEDOT charge storage counter-electrode and an ion-gel electrolyte was successfully obtained. The FE-SEM images of the photoanode showed the electrochemical growth of the ZnO nanorod arrays with a high degree of orientation along the z-axis. The HRTEM image of the Ag$_2$S quantum dots demonstrated that they covered the entire nanorod surface and had an average diameter of 10–20 nm. The presence of ZnS over Ag$_2$S was identified through XPS analysis. A symmetric supercapacitor based on PEDOT electrodes and PVP/[HEMIm][BF$_4$] electrolyte was developed as the charge storage part of the photo-supercapacitor. Its specific capacitance was 0.667 mF cm^{-2}, and the storage efficiency was 6.83%. The photosupercapacitor showed high stability with the photocharge and discharge cycles achieving a maximum voltage of 0.33 V in 40 s.

This configuration of the two-electrode photocapacitor offers an interesting starting point to improve the efficiency and reduce the cost of three-electrode photocapacitor production without employing dyes as sensitizers.

Conflicts of interest

There are no conflicts of interest to declare.

Acknowledgements

References

1 M. R. Lukatskaya, B. Dunn and Y. Gogotsi, *Nat. Commun.*, 2016, **7**, 1–13.

2 J. Liang, G. Zhu, Z. Lu, P. Zhao, C. Wang, Y. Ma, Z. Xu, Y. Wang, Y. Hu, L. Ma, T. Chen, Z. Tie, J. Liu and Z. Jin, *J. Mater. Chem. A*, 2018, **6**, 2047–2052.

3 V. Vega-Garita, L. Ramirez-Elizondo, N. Narayan and P. Bauer, *Prog. Photovoltaics Res. Appl.*, 2019, **27**, 346–370.

4 J. Xu, Z. Ku, Y. Zhang, D. Chao and H. J. Fan, *Adv. Mater. Technol.*, 2016, **1**, 1–5.

5 P. Simon and Y. Gogotsi, *Nat. Mater.*, 2008, **7**, 845–854.

6 N. Bagheri, A. Aghaei, M. Y. Ghotbi, E. Marzbanrad, N. Vlachopoulos, L. Häggman, M. Wang, G. Boschloo, A. Hagfeldt, M. Skunik-Nuckowska and P. J. Kulesza, *Electrochim. Acta*, 2014, **143**, 390–397.

7 D. Schmidt, M. D. Hager and U. S. Schubert, *Adv. Energy Mater.*, 2016, **6**, 1500369.

8 X. Xia, J. Luo, Z. Zeng, C. Guan, Y. Zhang, J. Tu, H. Zhang and H. J. Fan, *Sci. Rep.*, 2012, **2**, 981.

9 J. Xu, H. Wu, L. Lu, S. F. Leung, D. Chen, X. Chen, Z. Fan, G. Shen and D. Li, *Adv. Funct. Mater.*, 2014, **24**, 1840–1846.

10 J. Rodríguez-Moreno, E. Navarrete-Astorga, E. A. Dalchiele, R. Schrebler, J. R. Ramos-Barrado and F. Martín, *Chem. Commun.*, 2014, **50**, 5652–5655.

11 E. Navarrete-Astorga, J. Rodríguez-Moreno, E. A. Dalchiele, R. Schrebler, P. Leyton, J. R. Ramos-Barrado and F. Martín, *J. Solid State Electrochem.*, 2017, **21**, 1431–1444.

12 J. Rodríguez-Moreno, E. Navarrete-Astorga, E. A. Dalchiele, L. Sánchez, J. R. Ramos-Barrado and F. Martín, *J. Power Sources*, 2013, **237**, 270–276.

13 J. Rodríguez-Moreno, E. Navarrete-Astorga, E. A. Dalchiele, R. Schrebler, J. R. Ramos-Barrado and F. Martín, *Chem. Commun.*, 2014, **5652**, 5652–5655.

14 Y. Jin, Z. Li, L. Qin, X. Liu, L. Mao, Y. Wang, F. Qin, Y. Liu, Y. Zhou and F. Zhang, *Adv. Mater. Interfaces*, 2017, **4**, 1–8.

15 Y. Sun and X. Yan, *Sol. RRL*, 2017, **1**, 1700002.

16 E. Navarrete-Astorga, D. Solís-Cortés, J. Rodríguez-Moreno, E. A. Dalchiele, R. Schrebler, F. Martín and J. R. Ramos-Barrado, *Chem. Commun.*, 2018, **54**, 10762–10765.

17 R. Liu, Y. Liu, H. Zou, T. Song and B. Sun, *Nano Res.*, 2017, **10**, 1545–1559.

18 M. Yu, W. D. McCulloch, Z. Huang, B. B. Trang, J. Lu, K. Amine and Y. Wu, *J. Mater. Chem. A*, 2016, **4**, 2766–2782.

19 N. Vlachopoulos and A. Hagfeldt, in *Molecular Devices for Solar Energy Conversion and Storage*, Springer Nature, 2018.

20 T. Song and B. Sun, *ChemSusChem*, 2013, **6**, 408–410.

21 T. R. Cook, D. K. Dogutan, S. Y. Reece, Y. Surendranath, T. S. Teets and D. G. Nocera, *Chem. Rev.*, 2010, **110**, 6474–6502.

22 B. Luo, D. Ye and L. Wang, *Adv. Sci.*, 2017, **4**, 1–15.

23 J. Xu, Y. Chen and L. Dai, *Nat. Commun.*, 2015, **6**, 1–7.

24 R. Narayanan, P. N. Kumar, M. Deepa and A. K. Srivastava, *Electrochim. Acta*, 2015, **178**, 113–126.

25 C. Shi, H. Dong, R. Zhu, H. Li, Y. Sun, D. Xu, Q. Zhao and D. Yu, *Nano Energy*, 2015, **13**, 670–678.

26 N. Guijarro, J. M. Campiña, Q. Shen, T. Toyoda, T. Lana-Villarreal, R. Gómez and R. Go, *Phys. Chem. Chem. Phys.*, 2011, **13**, 12024–12032.

27 G. Guerguerian, F. Elhordoy, C. J. Pereyra, R. E. Marotti, F. Martín, D. Leinen, J. R. Ramos-Barrado and E. A. Dalchiele, *Nanotechnology*, 2011, **22**, 505401.

28 L. Campo, C. J. Pereyra, L. Amy, F. Elhordoy, R. E. Marotti, F. Martin, J. R. Ramos-Barrado, E. a. Dalchiele, F. Mart, F. Martín, J. R. Ramos-Barrado and E. a. Dalchiele, *ECS J. Solid State Sci. Technol.*, 2013, **2**, Q151–Q158.

29 P. V. Kamat, *Acc. Chem. Res.*, 2012, **45**, 1906–1915.

30 C. Chen, Y. Xie, G. Ali, S. H. Yoo and S. O. Cho, *Nanotechnology*, 2010, **22**, 15202.

31 Y. Chen, L. Wei, G. Zhang and J. Jiao, *Nanoscale Res. Lett.*, 2012, **7**, 1–6.

32 M. Shalom, S. Buhbut, S. Tirosh and A. Zaban, *J. Phys. Chem. Lett.*, 2012, **3**, 2436–2441.

33 J. Joo, D. Kim, D. J. Yun, H. Jun, S. W. Rhee, J. Sung Lee, K. Yong, S. Kim and S. Jeon, *Nanotechnology*, 2010, **21**, 325604.

34 H. Wang, T. Wang, X. Wang, R. Liu, B. Wang, H. Wang, Y. Xu, J. Zhang and J. Duan, *J. Mater. Chem.*, 2012, **22**, 12532–12537.

35 S. H. Im, H. J. Kim, S. Kim, S. W. Kim and S. Il Seok, *Org. Electron.*, 2012, **13**, 2352–2357.

36 H. Shen, X. Jiao, D. Oron, J. Li and H. Lin, *J. Power Sources*, 2013, **240**, 8–13.

37 M. M. Islam, A. T. Chidembo, S. H. Aboutalebi, D. Cardillo, H. K. Liu, K. Konstantinov and S. X. Dou, *Front. Energy Res.*, 2014, **2**, 1–11.

38 S. Dhar, T. Majumder, P. Chakraborty and S. P. Mondal, *Org. Electron.*, 2018, **53**, 101–110.

39 Y. Wang, P. Shao, Q. Chen, Y. Li, J. Li and D. He, *J. Phys. D: Appl. Phys.*, 2017, **50**, 175105.

40 B. Babakhani and D. G. Ivey, *Electrochim. Acta*, 2010, **55**, 4014–4024.

41 J. Rodríguez-Moreno, E. Navarrete-Astorga, F. Martín, R. Schrebler, J. R. Ramos-Barrado and E. A. Dalchiele, *Thin Solid Films*, 2012, **525**, 88–92.

42 V. González-Pedro, X. Xu, I. Mora-Seró and J. Bisquert, *ACS Nano*, 2010, **4**, 5783–5790.

43 M. Wang, C. Chen, H. Qin, L. Zhang, Y. Fang, J. Liu and L. Meng, *Adv. Mater. Interfaces*, 2015, **2**, 1–10.

44 T. Vdovenkova, A. Vdovenkov and R. Tornqvist, *Thin Solid Films*, 1999, **343–344**, 332–334.

45 D. Lin, H. Wu, R. Zhang, W. Zhang and W. Panw, *J. Am. Ceram. Soc.*, 2010, **93**, 3384–3389.

46 D. Briggs, C. D. Wanger, W. M. Riggs, L. E. Davis, J. F. Moulder and G. E. Muilenberg, *Handbook of X-ray photoelectron spectroscopy: a reference book of standard data for use in X-ray photoelectron spectroscopy*, PerkinElmer Corp., 1979.

47 W. Zhang, L. Zhang, Z. Hui, X. Zhang and Y. Qian, *Solid State Ionics*, 2000, **130**, 111–114.

48 R. G. Snyder and G. Zerbi, *Spectrochim. Acta A*, 1967, **23**, 391–437.

49 G. Louarn, J. P. Buisson, S. Lefrant and D. Fichou, *J. Phys. Chem.*, 1995, **99**, 11399–11404.

50 S. Garreau, G. Louarn, J. P. Buisson, G. Froyer and S. Lefrant, *Macromolecules*, 1999, **32**, 6807–6812.

51 P. Pfluger and G. B. Street, *J. Chem. Phys.*, 1984, **80**, 544–553.

52 D. H. Han, J. W. Kim and S. M. Park, *J. Phys. Chem. B*, 2006, **110**, 14874–14880.

53 J. S. Loring and W. Ronald Fawcett, *J. Phys. Chem. A*, 1999, **103**, 3608–3617.

54 X. Zhang, X. Huang, C. Li and H. Jiang, *Adv. Mater.*, 2013, **25**, 4093–4096.

55 P. J. Kulesza, M. Skunik-Nuckowska, K. Grzejszczyk, N. Vlachopoulos, L. Yang, L. Haggman and A. Hagfeldt, *ECS Trans.*, 2013, **50**, 235–244.

56 P. A. Mini, S. V. Nair and K. R. V. Subramanian, *Prog. Photovoltaics Res. Appl.*, 2012, **21**, 1153–1157.

57 A. Takshi, H. Yaghoubi, T. Tevi and S. Bakhshi, *J. Power Sources*, 2015, **275**, 621–626.

58 S. C. Lau, H. N. Lim, T. B. S. A. Ravoof, M. H. Yaacob, D. M. Grant, R. C. I. MacKenzie, I. Harrison and N. M. Huang, *Electrochim. Acta*, 2017, **238**, 178–184.

59 J. Bae, Y. J. Park, M. Lee, S. N. Cha, Y. J. Choi, C. S. Lee, J. M. Kim and Z. L. Wang, *Adv. Mater.*, 2011, **23**, 3446–3449.

60 J. Xu, H. Wu, L. Lu, S. F. Leung, D. Chen, X. Chen, Z. Fan, G. Shen and D. Li, *Adv. Funct. Mater.*, 2014, **24**, 1840–1846.

61 X. Huang, X. Zhang and H. Jiang, *J. Power Sources*, 2013, **248**, 434–438.

62 Y. Wang, J. Tang, Z. Peng, Y. Wang, D. Jia, B. Kong, A. A. Elzatahry, D. Zhao and G. Zheng, *Nano Lett.*, 2014, **14**, 3668–3673.

63 W. W. Chiu, J. Travaš-Sejdić, R. P. Cooney and G. A. Bowmaker, *J. Raman Spectrosc.*, 2006, **37**, 1354–1361.